Probability of rail break caused by out-of-round wheel loads

Downloaded from: https://research.chalmers.se, 2026-04-03 03:18 UTC

Citation for the original published paper (version of record):
Nielsen, J., Ekberg, A. (2023). Probability of rail break caused by out-of-round wheel loads. Engineering Structures, 294. http://dx.doi.org/10.1016/j.engstruct.2023.116717

N.B. When citing this work, cite the original published paper.

research.chalmers.se offers the possibility of retrieving research publications produced at Chalmers University of Technology. It covers all kind of research output: articles, dissertations, conference papers, reports etc. since 2004. research.chalmers.se is administrated and maintained by Chalmers Library

(article starts on next page)

Engineering Structures 294 (2023) 116717

Contents lists available at ScienceDirect

Engineering Structures

journal homepage: www.elsevier.com/locate/engstruct

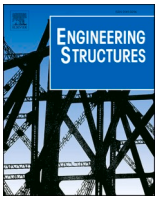

Probability of rail break caused by out-of-round wheel loads

Jens C.O. Nielsen *, Anders Ekberg

Department of Mechanics and Maritime Sciences / CHARMEC, Chalmers University of Technology, SE-412 96 Gothenburg, Sweden

ARTICLE INFO

Keywords:
Rail break probability
Out-of-round wheel
Wheel-rail impact
Linear elastic fracture mechanics
Dynamic vehicle-track interaction
Poly-harmonic spline
Subset simulation algorithm

ABSTRACT

A simulation procedure to predict the probability of rail break due to a measured wheel load spectrum is presented. The load distribution includes a representative proportion of high-magnitude dynamic loads generated by out-of-round wheels. Linear elastic fracture mechanics is applied to determine the stress intensities of pre-existing rail head cracks in a continuously welded rail subjected to combined bending and temperature loading. Rail bending moments are evaluated using a validated time-domain model of dynamic vehicle–track interaction. The considered multi-dimensional stochastic parameter space includes field test data of dynamic loads from a wheel impact load detector and crack depths from eddy current data. Meta-models based on poly-harmonic splines are applied to reduce the computational cost of the analysis. Supported by the extensive field test data, the simulation procedure is demonstrated by investigating the influences of freight traffic type, track support stiffness and rail temperature on the probability of a rail break initiated at a pre-existing rail head crack.

1. Introduction

Statistics between 2016 and 2020 for the Swedish railway network indicate that the number of rail breaks per year is decreasing. Still, in 2020, 52 rail breaks were reported. Most of these occurred during winter, with at least one third appearing at rail welds. Apart from weld failures, many rail breaks are caused by rolling contact fatigue (RCF) commonly in the form of head checks initiated at the gauge corner (see Fig. 1), and by squats initiated towards the top of the rail head. As the crack deviates to transverse growth at a depth of about 4 mm, propagation is driven by cyclic bending and static tensile thermal stresses caused by a low ambient temperature and the restricted contraction of continuously welded rails. For these long cracks, both frictional stresses and the resulting heating of the rail head will have less influence since their stress magnitude decreases rapidly with depth from the surface. Growth rates increase as the crack approaches final fracture. In broken rail specimens, this can be seen as sparser beach marks at the end of the propagation stage, see Fig. 1. Final fracture typically occurs when large parts of the rail head is cracked as in Fig. 1, but can be triggered also by smaller cracks, e.g., in secondary fractures during derailments [1,2].

Head checks predominantly occur in fairly wide curves (under current conditions with radii of around 500–1000 m), whereas squats are more common on tangent track. Inspections to identify these cracks typically employ ultrasonic [3] or eddy current testing, although other possibilities exist [4]. The inspection is complicated by the fact that deep cracks may be shielded by an overlying network of more shallow cracks [5]. Smaller cracks are removed by grinding, whereas larger cracks may require extensive milling or rail replacement.

Wheel–rail impact loads generated by discrete wheel tread surface irregularities (e.g., due to wheel flats or material fall-out from clusters of rolling contact fatigue cracking) increase the risk of rail breaks and may also cause severe damage of track and vehicle components leading to high maintenance costs and traffic disruptions. Examples of secondary damage include failure of prestressed concrete sleepers, where the influence of repeated impact loading resembling the influence of wheel flats has been studied in laboratory conditions [6], and failure of rail fastenings as investigated in [7]. In addition, wheelsets and running gear are susceptible to damage and failures due to repeated impact loading. For example, the influence of wheel out-of-roundness on wheel–rail interaction and the fatigue life of railway wheels has been studied in [8–10].

Wheel impact load detectors (WILDs) are used to monitor vertical wheel–rail contact forces generated by out-of-round wheels. Alarm limits for (maximum) wheel loads are prescribed to prevent failures that may have safety implications. The UIC recommended alarm limit for peak wheel load proclaims an immediate stop of the train at 350 kN with an alert level at 300 kN [11]. For continuously welded rails in areas with particularly cold winters, an alarm limit dependent on temperature relative to the stress-free rail temperature is advisable. Understanding the influence of out-of-round wheels on the risk for track damage

* Corresponding author.
E-mail address: jens.nielsen@chalmers.se (J.C.O. Nielsen).

https://doi.org/10.1016/j.engstruct.2023.116717
Received 17 April 2023; Received in revised form 28 June 2023; Accepted 30 July 2023
Available online 7 August 2023
0141-0296/© 2023 The Author(s). Published by Elsevier Ltd. This is an open access article under the CC BY license (http://creativecommons.org/licenses/by/4.0/).

Fig. 1. Head check crack (initiation top left) propagating to transverse growth and causing a rail break (light grey area indicating final fracture).

(particularly instant rail breaks) was the scientific basis for the specification of the current alert levels and alarm limits.

In this study, the probability of an instant rail break initiated at a pre-existing rail head crack due to severe wheel impact loading is investigated. The railhead crack is considered long enough to have deviated to transverse growth. The propagation of the crack is thus assumed to be driven by combined bending and temperature loading. It is shown that the maximum tensional stress in the rail head crack is generated if the wheel impact occurs while the crack is positioned in between the two adjacent wheels in a bogie (or in between two facing wheels in two adjacent vehicles). The presented simulation procedure includes applications of field test data, statistical methods considering a multi-dimensional stochastic parameter space, and a validated time-domain model for simulation of dynamic vehicle-track interaction. Meta-models based on poly-harmonic splines are applied to reduce the computational cost of the analysis. A similar study investigating the risk of rail break initiated at a rail foot crack and limited to two stochastic parameters was presented in an earlier paper [12]. It should be noted that rail foot cracks are more straightforward to analyse in the sense that the maximum tensional stress is generated if the impact occurs when the wheel is directly above the crack. As mentioned, the study features a single crack, which is a simplification of the real situation especially for head checks where multiple cracks typically exist along the rail. In general terms, multiple cracks may decrease the crack loading due to crack tip shielding effects. Once a rail break occurs, it will however significantly increase the risk of multiple rail breaks, which poses a major derailment risk.

2. Wheel–rail impact – measurements

To illustrate the influence of discrete wheel tread surface damage on dynamic wheel–rail contact forces and rail bending moment, examples from extensive field measurements on two different railway lines will be briefly discussed.

2.1. Svealandsbanan

The influence of wheel out-of-roundness (OOR) on dynamic loads was investigated in an extensive field measurement campaign conducted in 2000 [13] on the Swedish track corridor *Svealandsbanan*. The tests were performed on tangent track comprising 60E1 rails, 10 mm studded rubber rail pads, and concrete monobloc sleepers on a ballast bed. The mean sleeper distance was 0.65 m.

Different types of wheel tread surface irregularities were introduced in the running gear of a test train. Strain gauges were mounted on the rail web in nine consecutive sleeper bays to measure wheel–rail contact forces. Strain gauges on the rail foot were mounted at 11 locations along the track to measure rail bending moment at mid-span and above sleepers. For each train passage, time histories from 40 channels were recorded with a sampling frequency of 6 kHz. Axle loads were in the order of 25 tonnes and train speeds were varied.

Fig. 2 (top) shows part of the measured wheel–rail contact force time history in one sleeper bay as generated by the loaded test train passing at 100 km/h. The bogie wheelbase was 1.8 m, and the distance between facing wheelsets in two adjacent freight vehicles was 3.4 m. For each passing wheel, the measured contact force increases from zero to around the static wheel load when an undamaged wheel enters the instrumented section of the sleeper bay. The third wheel (radius 0.44 m) had a 60 mm wheel flat with depth 1 mm. After the wheel–rail contact has reached the leading edge of the flat, there is a reduction in contact force due to the local deviation in wheel radius (around 2.98 s). In this example, the contact force was not reduced to zero, implying no loss of wheel–rail contact. After passing the centre of the wheel flat, the wheel continues downwards forcing the rail to do the same. In this case, this resulted in an impact load of 230 kN. Note that the same flat generated impacts also at around 2.88 s and 3.08 s.

The two lower diagrams in Fig. 2 illustrate the measured rail bending moment at two sleeper bay centra located two sleeper bays apart. The bending moment is dominated by the influence of the quasi-static load from the passing wheels. However, significant transient contributions are generated by the wheel flat. The middle figure shows the impact close to the instrumented position generating a significant contribution to the positive rail bending moment (tension in the rail foot) when the wheel is passing the sensor. Almost simultaneously the impact is indicated by the sensor two sleeper bays away (bottom figure), which at this time instant is at a position between two adjacent wheels. Here the wheel impact is generating a substantial contribution to the negative rail bending moment. If there is a pre-existing rail head crack at this location, an instant rail break can be triggered if the stress intensity of the loaded crack exceeds the fracture toughness of the rail.

2.2. Malmbanan

Malmbanan is a single-track railway line in the northern part of Sweden. Traffic is dominated by iron ore trains with axle loads up to 32.5 tonnes (speed 60 km/h), and other freight trains with axle loads up to 25 tonnes (speeds up to 120 km/h). In winter, weather conditions can be severe including snowstorms and temperatures down to some –40 °C.

For two categories of traffic (iron ore trains and freight trains from a specified operator), data from the WILD at *Sunderbyn* measured over six months between 1 October 2017 and 1 April 2018 have been assessed, see Fig. 3 and [12]. In Fig. 4, the distributions of peak loads and axle loads are shown. The range of each axle load bin is 2.5 tonnes, while the range of each peak load bin is 5 kN. Peak loads were generally higher for the freight traffic despite the significantly lower axle loads compared to iron ore wheels. Several of these wheels exceeded the alarm limit of 350 kN with a maximum peak load of 455 kN. This indicates that several of the freight wheels were in worse condition compared to the wheels in the iron ore fleet.

For all iron ore and freight wheels with axle loads $\geq$ 27.5 tonnes and $\geq$ 20 tonnes, respectively (corresponding to loaded wagons) measured in March 2018, cumulative spectra of the dynamic loads based on the three-parameter Burr type XII distribution are shown in Fig. 5. The dynamic loads were evaluated by subtracting the measured mean wheel load from the measured peak load. For comparison, about 1 permille of the passing freight wheels generated dynamic loads exceeding 170 kN,

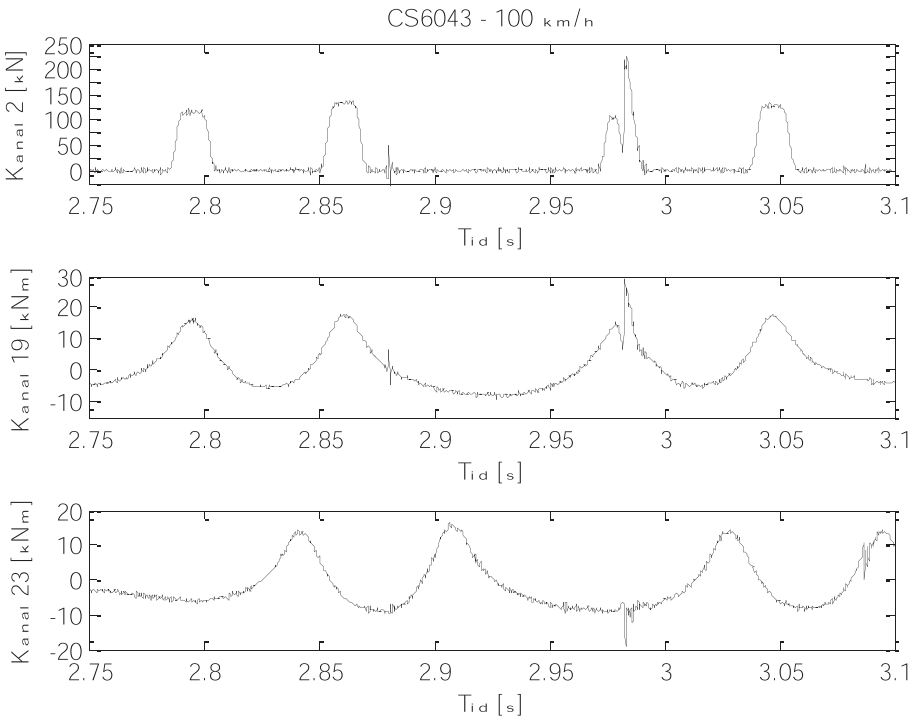

Fig. 2. Measured time histories of (top) wheel–rail contact force in one sleeper bay, (middle and bottom) rail bending moment at two sleeper bay centra two sleeper bay distances apart. 'Tid' and 'Kanal' mean time and channel, respectively. From [14].

Fig. 3. Wheel impact load detector at Sunderbyn on Malmbanan [15]. Rail seat loads are measured at eight consecutive sleepers. Photo by Matthias Asplund, Swedish Transport Administration.

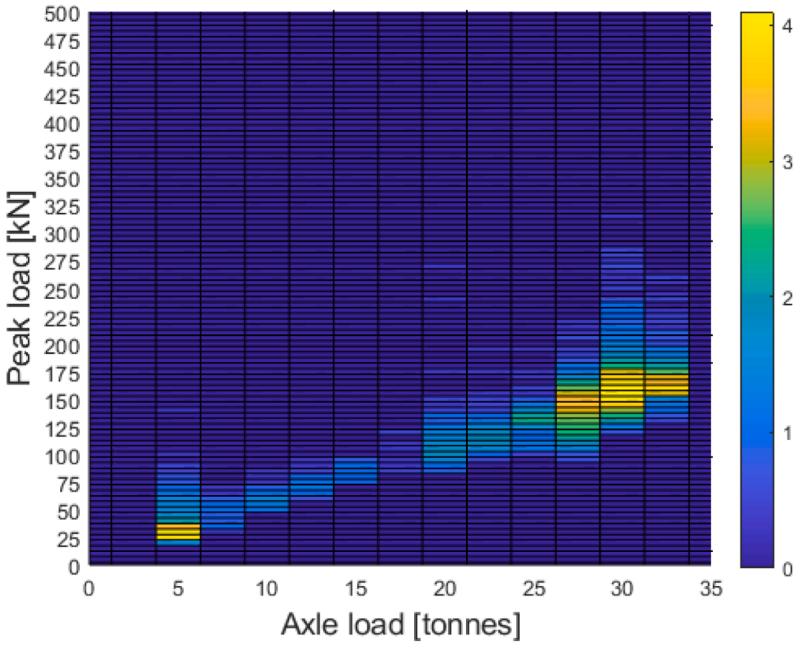

(a)

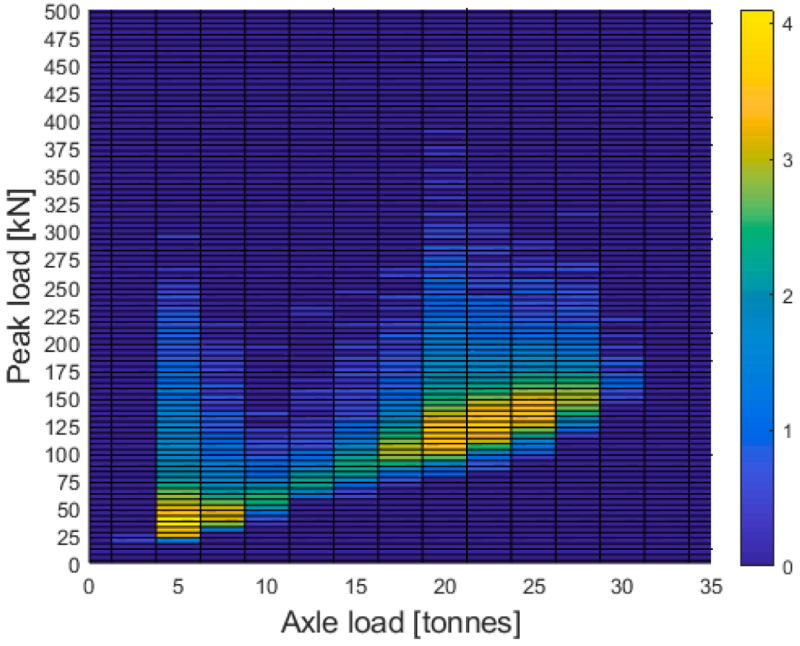

(b)

Fig. 4. Wheel impact load detector data from Sunderbyn: 1 October 2017 – 1 April 2018. Colour bar indicates number of occurrences in 10-logarithm scale; for example, 4 corresponds to 10^4 wheels. (a) iron ore (total of 197 800 wheels), (b) freight (126 771 wheels).

while only 0.4 permille of iron ore wheels generated dynamic loads exceeding 100 kN.

The cumulative Burr type XII distribution for a given stochastic variable θ is written as [16]

$$\Phi_{\mathrm{B}}(\theta|\alpha,c,k)=1-\frac{1}{\left\{1+\left(\frac{\theta}{\alpha}\right)^{c}\right\}^{k}},\theta>0,\alpha>0,c>0,k>0 \tag{1}$$

where c and k are shape parameters, while α is a scale parameter. For an assessment of the matched tail distribution of extreme dynamic loads, note that the fitted Burr type XII distribution for the 'freight operator' wheels predicts that 5 permille of the dynamic loads exceed 170 kN, while the prediction for the iron ore wheels is that 1.6 permille exceed 100 kN. Thus, for both vehicle types, the load distributions that will be applied in Section 6 for a demonstration of the risk analysis procedure

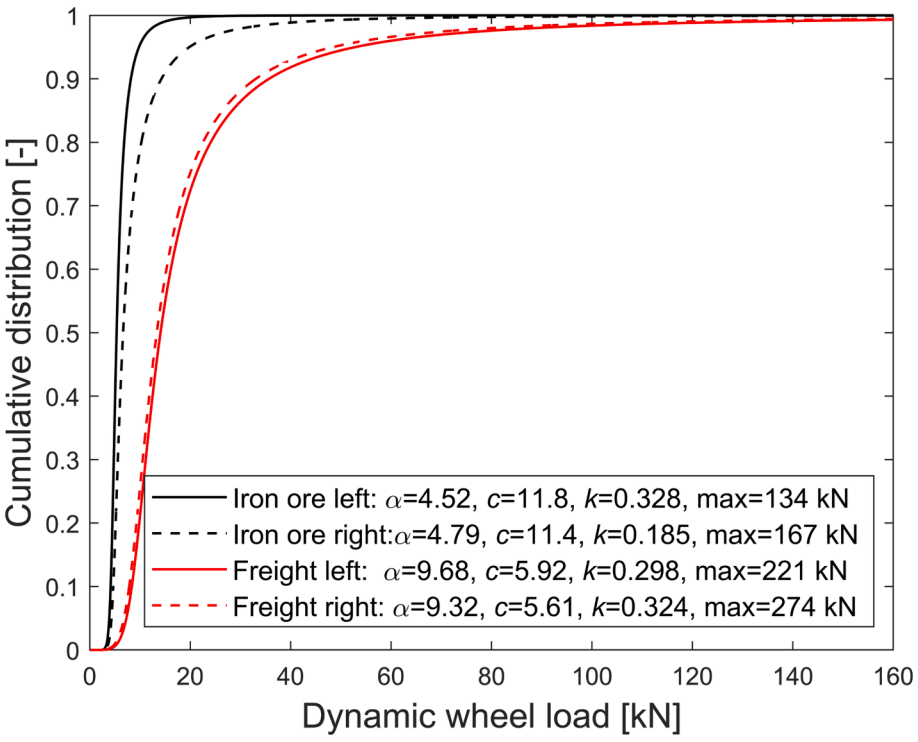

Fig. 5. *Cumulative Burr type XII distributions of dynamic wheel load measured at Sunderbyn from 1 March 2018 – 1 April 2018. For each distribution (iron ore wagons with axle loads* $\geq$ 27.5 tonnes*: 17 855 (left and right) wheels, freight operations with axle loads* $\geq$ 20 tonnes*: 9390 wheels), the distribution parameters and maximum measured load are given in the legend.*

will be conservative.

3. Fracture mechanics analyses

To evaluate stress intensities at rail head cracks subjected to bending and thermal loading, linear elastic fracture mechanics (LEFM) is employed [17,18]. The crack geometry is given in Fig. 6. A single gauge corner crack is considered meaning that the influence of any nearby (in the rail direction) cracks is ignored. Further, the influence of residual stresses is neglected motivated by the fact that in the vicinity of a propagating fatigue crack the residual stress field is reduced and redistributed compared to the case for an uncracked rail, cf. [17,19].

Presuming Euler–Bernoulli beam theory to be valid, a time-variant rail bending moment M_y corresponds to a time-variant normal stress σ_B in the rail head as

$$\sigma_B(t) = -M_y(t)\cdot h_h / I_y \tag{2}$$

with the sign convention that a negative bending moment generates a tensile stress in the rail head. Further, I_y is the cross-sectional moment of inertia and h_h the vertical distance from the neutral axis to the top of the head, as defined in Fig. 6. The uniform normal stress due to restricted thermal contraction (compression) in the continuously welded rail is evaluated as

$$\sigma_T = E\alpha_T \Delta T \tag{3}$$

where $E = 210$ [GPa] is the Young's modulus and $\alpha_T = 11.5{\cdot}10^{-6}$ [°C^{-1}] is the thermal expansion coefficient. The rail temperature difference $\Delta T = T_0 - T$, where T_0 is the stress-free temperature and T is the ambient rail temperature. Note here that T_0 may differ from the nominal stress-free temperature e.g., due to movements of rail. The mode I stress intensity factor due to bending and temperature loads at the rail head crack is derived through superposition as

$$K_I(a_h, b_h, t) = f_B(a_h, b_h)\cdot\sigma_B(t)\sqrt{\pi a_h} + f_T(a_h, b_h)\cdot\sigma_T(t)\sqrt{\pi a_h} \tag{4}$$

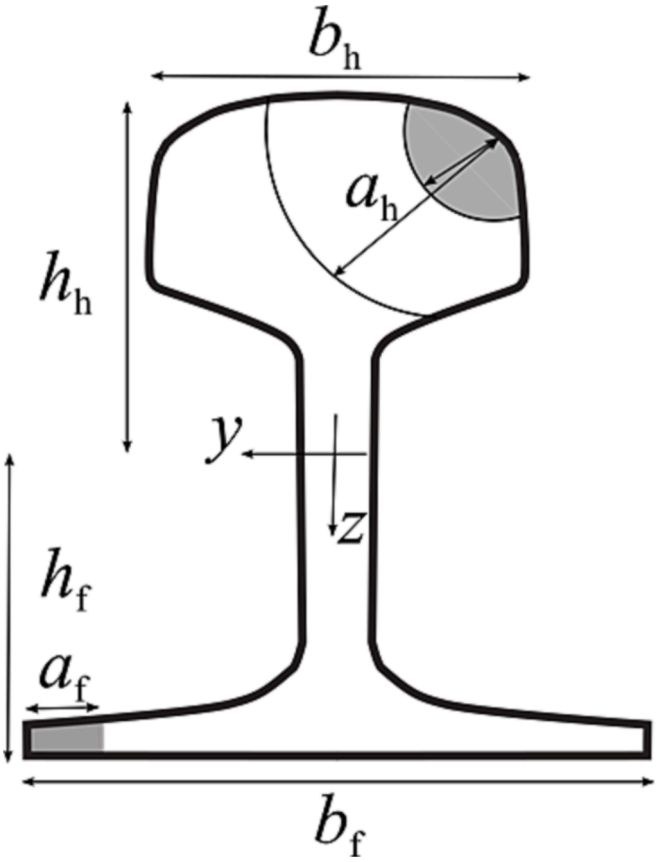

Fig. 6. Geometry of the studied rail head crack. For a nominal 60E1 rail profile, $I_y = 30.55{\cdot}10^{-6}$ m^4, $h_h = 0.091$ m and $b_h = 0.072$ m.

Here a_h is the crack depth as defined in Fig. 6. For a head check crack in a 60E1 rail, the geometry factors for bending and tension can be approximated, [17], as

$$f_B(a_h, b_h) = 0.70 - 0.97\left(\frac{a_h}{b_h}\right) + 2.60\left(\frac{a_h}{b_h}\right)^2 \quad (5a)$$

$$f_T(a_h, b_h) = 0.72 - 0.16\left(\frac{a_h}{b_h}\right) + 1.40\left(\frac{a_h}{b_h}\right)^2 \quad (5b)$$

Fracture occurs when

$$\max_t\{K_I(t)\} \geq K_{Ic} \quad (6)$$

where K_{Ic} is the fracture toughness of the rail material. The bending moment and the corresponding part of the combined stress intensity are evaluated at each wheel passage based on simulations of dynamic vehicle–track interaction, see Section 4. Since the bulk rail temperature is constant during a wheel passage, $\max_t\{K_I(t)\}$ is occurring when the rail bending moment induced by the wheel passage is minimum.

In general, fracture as defined by the fulfilment of Equation (6) need not result in complete disintegration of the rail. However, for the current case a rail break will often occur since the bending stress gradient is rather shallow and the thermal stress magnitude often substantial. Note that a single rail break usually does not cause a derailment [19]. It is however a safety issue, may result in secondary damage, and will cause traffic disruptions as the rail needs to be repaired before traffic can be resumed.

Lateral bending and torsion are not accounted for in Equation (6). For a rail position between two wheels, lateral bending will contribute to the tensional stress at the rail gauge corner. For the curve radius interval studied here, see Section 4, lateral wheel–rail contact forces should be in the order of at least a factor 10 lower than the vertical forces, in particular when compared to situations with vertical impact loading. Indeed, the moment of inertia for bending in the lateral direction is significantly lower than for bending in the vertical direction, but the distance from the load to the neutral axis is relatively short. Torsion should have a small effect judging from fracture morphologies, which generally show little or no influence of shear. Altogether, for the studied conditions, it is reasonable to assume that the vertical bending together with thermal loading will dominate. These are also the parameters that are being measured and controlled in operations.

4. Crack depth, fracture toughness and track stiffness

Based on eddy current measurements, the statistical distribution of rail head crack depths has been determined for different curve radius intervals in a given track corridor on *Malmbanan*. Here, crack depths are quantified by maximum crack depth per metre track.

According to measurements performed in spring 2020, head checks were most prevalent in curves with radius in the interval 500 – 700 m. Cumulative (empirical) distributions of crack depth in three curve radius intervals are presented in Fig. 7. For more than half of the total track length in these curve radius intervals, it is observed that no head checks were detected. The curve radius interval with the most severe distribution of cracks is 500 – 600 m. Here, the total number of samples with crack depth $\geq$ 5 mm was 91 corresponding to about 1.2% of the total number of samples.

The maximum detectable crack depth is 5 mm implying that a deeper crack will be recorded as a 5 mm crack. To account for a reasonable distribution of crack depths larger than 5 mm, it is assumed that the cumulative distribution in Fig. 7 can be extrapolated. This has been achieved by assuming that the additional depth (added to the registered 5 mm) of these 91 cracks had an exponential distribution with a factor of 1.5. 10 samples of the exponential distribution have been considered in the simulations reported in Section 6. The largest crack depth in the cumulative distribution generated by these samples was 10.6, 10.8, 11.3, 15.0, 11.8, 11.2, 10.8, 13.8, 11.7, and 11.0 mm. Based on the cumulative distributions applied in the simulations, one such extreme crack per metre track would occur with a probability of about 0.13 permille.

Further, based on laboratory measurements according to EN13674-1 at rail temperature –20 °C, the fracture toughness for the rail head of rail

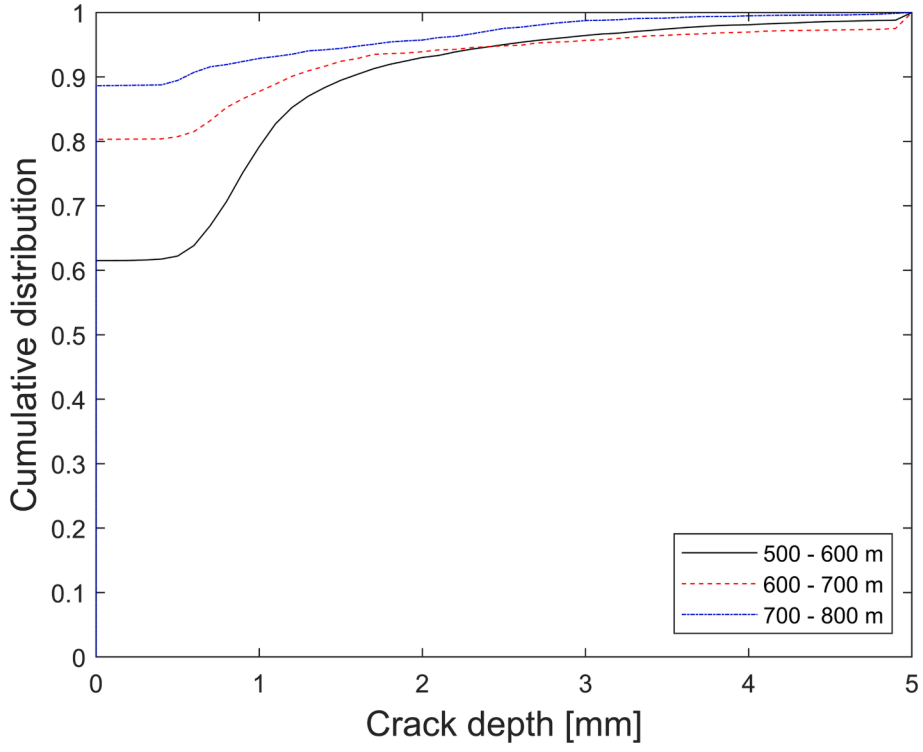

Fig. 7. Cumulative distributions of maximum crack depth per metre track based on eddy current measurements on Malmbanan track corridor 111 in spring 2020.

grade R350LHT can be approximated by a normal statistical distribution $N(35.3,\ 1.90)$ MPa·m$^{1/2}$[20]. Fracture toughness and fatigue crack growth rate tests for rail steels and thermite weld materials are also reported in [21].

Track stiffness has been measured on several sections of *Malmbanan* using the track geometry recording car IMV200 instrumented with lasers measuring rail deflection at several distances from one of the wheels [22]. It was concluded that the variation in stiffness was significant. In general, the support stiffness measured in autumn 2016 was relatively low indicating a soft subgrade. For one specific 4 km section of track, it was reported that the mean value and standard deviation of the rail support stiffness per rail side was 35 and 14 (kN/mm)/m, respectively. In Section 6, different deterministic (uniform) ballast/subgrade stiffnesses will be considered to illustrate its influence. However, treating the ballast/subgrade stiffness as another stochastic variable in the simulation procedure would be straightforward, cf. Section 5.4.

5. Simulation procedure

Based on a statistical distribution of dynamic wheel loads, the applied procedure for predicting the probability of an instant rail break from a pre-existing rail head crack is illustrated in Fig. 8. Traffic data and examples of distributions of dynamic loads measured in a WILD were presented in Section 2. The other steps in the procedure are described in the following sub-sections.

5.1. Baseline vehicle–track interaction model

For numerical simulations of high-magnitude impact loading in situations with potential loss of wheel–rail contact, a non-linear wheel–rail contact model is required. This means that the simulation of dynamic vehicle–track interaction needs to be carried out in the time domain [23]. In this paper, time histories of vertical dynamic wheel–rail contact force and rail bending moment are solved using DIFF [24]. A sketch of the applied baseline model is shown in Fig. 9. The model has previously been validated using an instrumented wheelset [25], and good agreement between calculated and measured rail bending moments has been obtained with a calibrated track model [14]. The same type of model was applied in a recent paper investigating the risk of failure due to a pre-existing rail foot crack [12]. A brief summary of the model is provided in this paper, while full details on model implementation are given in [24].

For simulation of wheel–rail impact loads, it is generally sufficient that the vehicle model includes only the wheelset (i.e. the unsprung mass) since the primary suspension isolates the bogie and carbody from the wheelset at frequencies above some 20 Hz. The remaining part of the vehicle can be represented by a static wheel load W. Here, a wheelset model containing two degrees of freedom is used, see Fig. 9[25,26]. The mass $M_w = 712.5$ kg corresponds to the unsprung mass of half of a SJ57H freight wheelset with wheel radius $R_w = 0.45$ m, which is a type of wheelset that is representative for the freight traffic described in Section 2.2. The non-physical parameters ($m_w = 3$ kg, $k_w = 1650$ kN/mm and $c_w = 5.4$ kNs/m) have been tuned using a detailed FE model of the wheelset[27]. Two wheelsets are included in the model since the

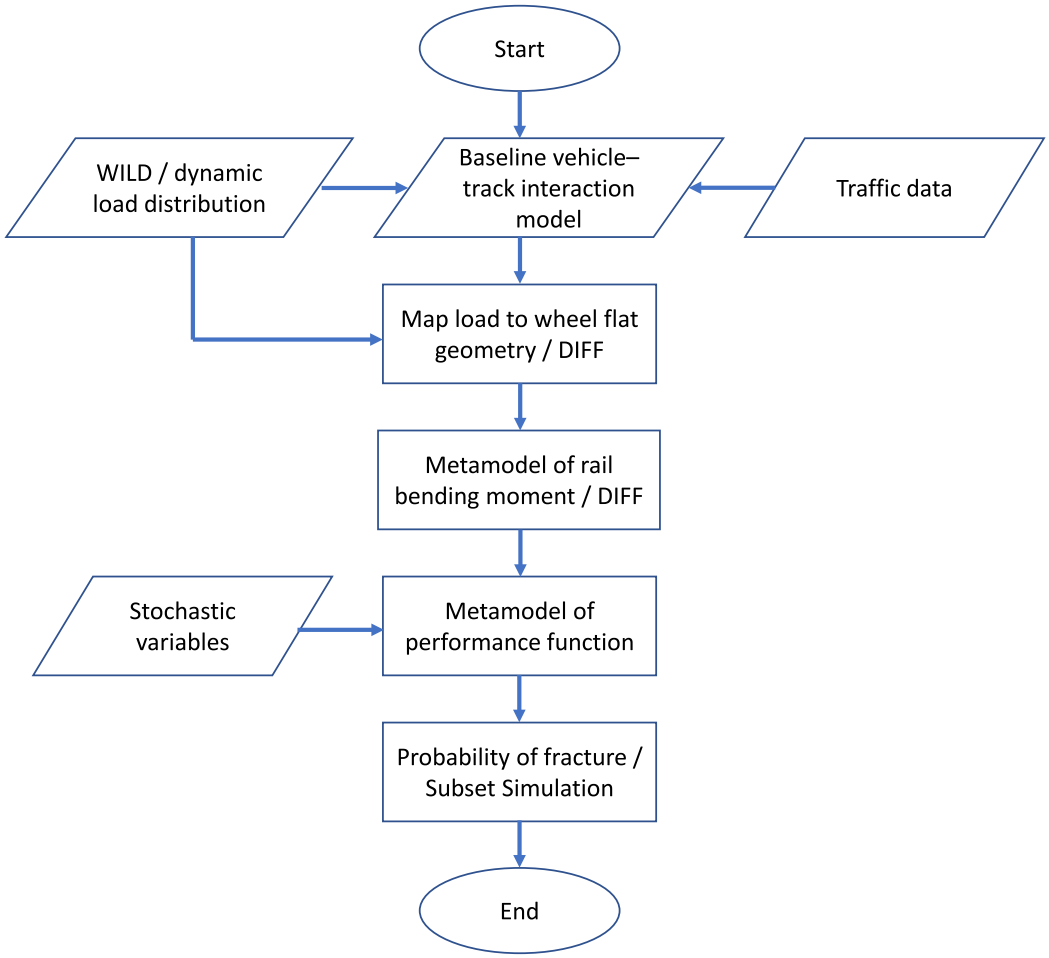

Fig. 8. Simulation procedure.

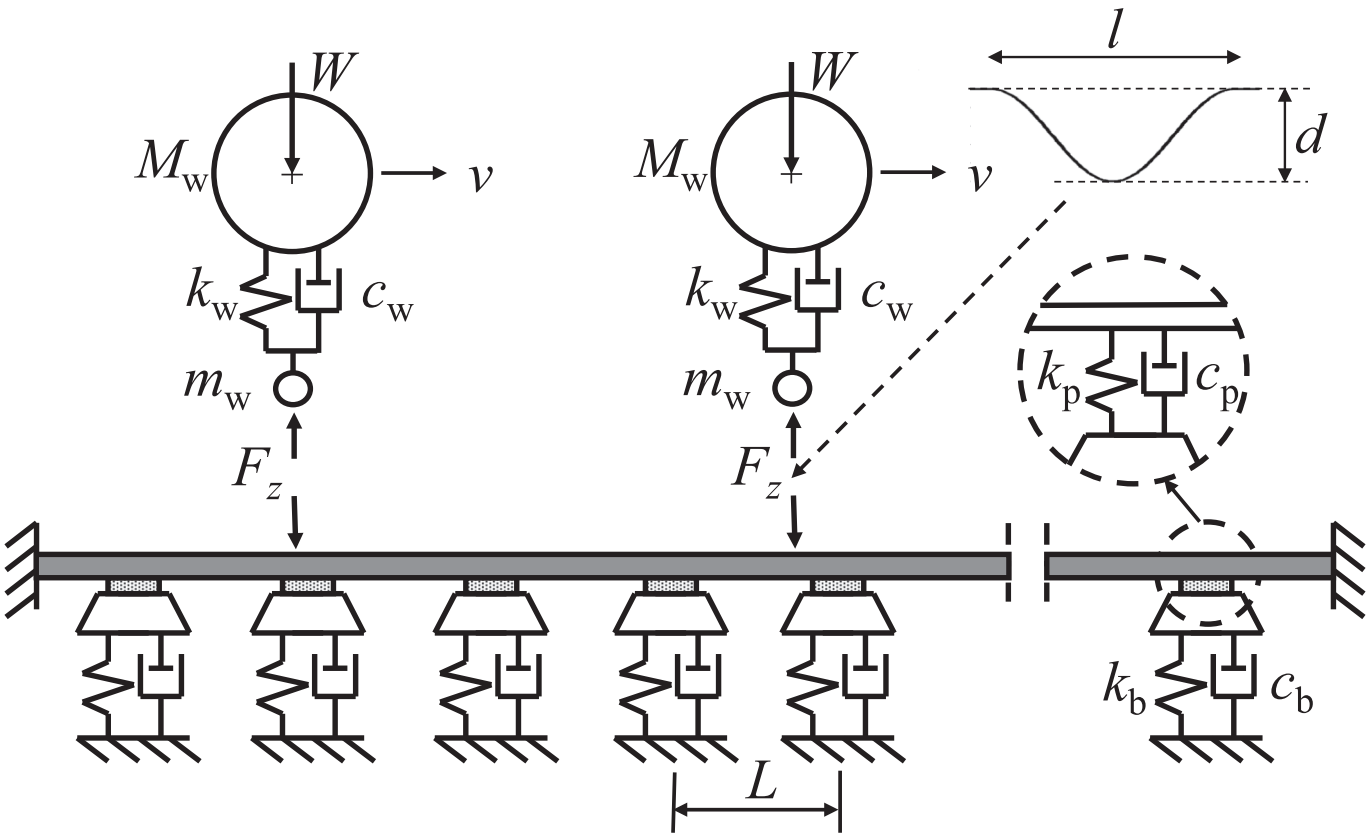

Fig. 9. Model for simulation of vertical dynamic vehicle–track interaction accounting for tread irregularity with length l and depth d on the leading wheel.

maximum tensional stress in the rail head is generated at a position between two adjacent wheelsets. It was found (not shown here) that the influence of adding more wheelsets than these two in one bogie was small. The distance between the two wheelsets is 1.8 m.

The track model includes one discretely supported 60E1 rail modelled by Rayleigh–Timoshenko beam theory. Each rail pad is described by a Kelvin model, while each half sleeper is represented by a discrete rigid mass. The combined vertical stiffness and damping of the ballast and subgrade below each sleeper are represented by another Kelvin model. The full track model contains 70 sleeper bays with clamped ends at both rail boundaries. Input data to the baseline track model are taken from[25]. The model has been validated (not shown here) versus impact hammer measurements in the *Sunderbyn* WILD. However, in those measurements, the detector was not pre-loaded by a vehicle resulting in lower stiffnesses for rail pads and ballast/subgrade. Aiming to represent the conditions in the *Sunderbyn* WILD when subjected to a loaded freight vehicle, the following input data have been employed for the baseline track model, cf. Fig. 9: rail pad stiffness k_p = 120 kN/mm, viscous rail pad damping c_p = 25 kNs/m, ballast/subgrade stiffness k_b = 60 kN/mm, viscous ballast/subgrade damping c_b = 49 kNs/m, sleeper spacing L = 0.60 m, and half sleeper mass 150 kg. This would correspond to a rail support stiffness of 67 (kN/mm)/m, which is stiffer than the mean value reported in Section 4 for other sections on *Malmbanan*, but still in a reasonable range for a WILD with proper support conditions.

To reduce the simulation time for dynamic vehicle–track interaction, the track model is taken as linear and a complex-valued modal approach with a truncated mode set is applied. Modes up to about 2.6 kHz, and a residual term to account for the influence of the truncated modes on rail bending moments, were considered.

As in [12], it is assumed that all dynamic wheel–rail contact loads are generated by the same geometrical shape of wheel tread surface irregularity, which can be described by a simple mathematical expression in one dimension, see Fig. 9. To this end, it is noted that the length l_0 and depth d of a new wheel flat with sharp edges are approximately related by

$$l_0 \approx \sqrt{8R_w d} \tag{8}$$

Wear and plastic deformation from repeated wheel–rail impacts tend to round the edges of a wheel flat while the depth remains similar. The radial wheel profile deviation x_{rf} for a flat with rounded edges and length l is approximated as, [28],

$$x_{rf} = \frac{d}{2}\left\{1+\cos\left(\frac{2\pi z}{l}\right)\right\}, \; -\frac{l}{2} \le z \le \frac{l}{2} \tag{9}$$

where z is an arc coordinate along the flat. In this paper, it is assumed that the depth of a new and rounded flat is the same but $l = 1.5 \cdot l_0$. The vertical trajectory of the wheel centre differs from the shape of the flat due to the curvature of the wheel. In this paper, the prescribed relative wheel–rail displacement x_w used as input to the dynamic vehicle–track interaction model is expressed as, [26],

$$x_w \approx \begin{cases} 4d\{(2z+l)/2l\}^2, & -l/2 \le z \le 0 \\ 4d\{(l-2z)/2l\}^2, & 0 \le z \le l/2 \end{cases} \tag{10}$$

For rounded wheel flats, it has been concluded that the Hertzian wheel–rail contact model with the prescribed relative wheel–rail displacement excitation used here generates results that are in good agreement with a more advanced three-dimensional contact model [29].

For each given combination of vehicle, track and excitation input, the simulation model is applied to calculate the time history of the vertical wheel–rail contact force $F_z = W + F_{dyn}$, where W is the static wheel load (half axle load) and F_{dyn} is the dynamic contribution to the force, cf. Fig. 9. The DIFF model could be further improved by implementing load-dependent properties for ballast and rail pad stiffnesses [30], but this is considered outside the scope of this paper.

5.2. Influence of impact position

The simulation model described in Section 5.1 has been applied to evaluate the influence of wheel flat depth d and ballast stiffness on the dynamic contribution F_{dyn} to the total wheel–rail contact force. For each depth d, Eqs. (8) and (10) with $l = 1.50 \cdot l_0$ were used to formulate the prescribed excitation input. The simulation was repeated for eight prescribed impact positions equidistantly distributed within one sleeper bay. In each case, the (longitudinal) centre of the tread irregularity was aligned with the prescribed impact position (although the actual impact position will occur towards the trailing end of the irregularity). Calculated mean values and standard deviations of the dynamic load are presented in Fig. 10(a). The baseline vehicle model featured a train speed of $v = 100$ km/h and a static wheel load of $W = 10$ tonnes. This is representative for regular freight traffic wheels measured in the WILD, cf. Fig. 4. It is observed that the influence of impact position (within a sleeper bay) on the evaluated impact load is significant and increases with increasing flat depth, cf. [29]. Further, it was concluded (not shown here) that the highest impact loads were generated when the impact occurred near a sleeper where the track stiffness at rail level is higher than elsewhere in the sleeper bay. For the same tread defect and vehicle speed, it has also been observed (not shown here) that the dynamic load F_{dyn} decreases with increasing axle load. In particular, loss of wheel–rail contact is less common at higher axle loads.

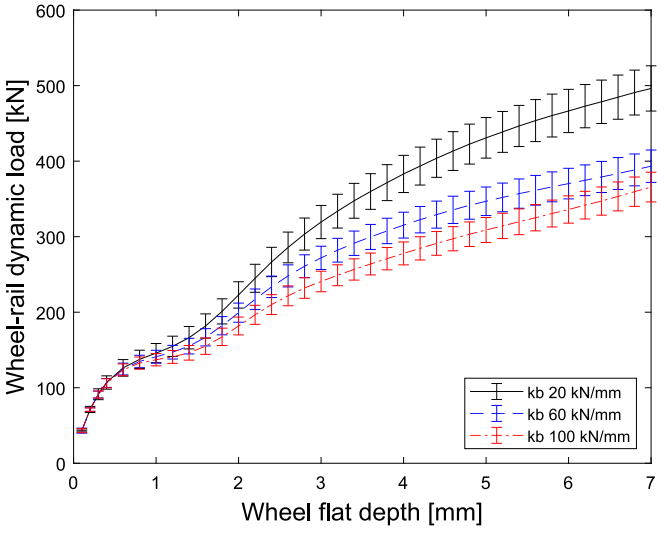

Fig. 10. Influence of wheel flat depth and ballast stiffness on mean value and standard deviation of (a) wheel–rail dynamic load and (b) minimum rail bending moment. For each wheel flat depth, eight impact positions within a sleeper bay were studied. Axle load 20 tonnes, train speed 100 km/h.

For each load case, the minimum rail bending moment (maximum tensional stress in the rail head) was evaluated from calculations of bending moment in cross-sections along the rail with a resolution of $L/64$. The minimum rail bending moments (considering all cross-sections and all impact positions) are shown in Fig. 10(b). For most track input data, the minimum rail bending moment was generated at a position that was close to the centre between the two wheels in the model. However, for very low ballast stiffnesses, the minimum bending moment occurred outside of the wheelbase at some distance from the wheel generating the impact. From the smaller standard deviation in Fig. 10 (b), it is seen that the influence of impact position on minimum rail bending moment is not as significant as for the dynamic load. The influence of impact position on minimum rail bending moment also decreases with increasing ballast stiffness.

The minimum bending moment along the rail has been calculated with a sampling distance of $L/64$ for $k_b = 60$ kN/mm and a wheel flat with $d = 1$ mm. Impact at four different locations in a sleeper bay have been considered. Results are presented in Fig. 11. As in Fig. 10(b), Fig. 11 illustrates the relatively small influence of impact position on the minimum rail bending moment (compare the magnitude of the four maxima), but also that the minimum rail bending moment remains within 90% (dashed horizontal lines) of the magnitude within a window of about 0.5 m. This means that the influence of the distance between the impact position and the considered crack is small as long as the distance between cracks is relatively short as can be expected for a rail section with several head checks.

Based on the results in Figs. 10 and 11, it is argued that the crack position within the sleeper bay, as well as the impact position relative to the position of the crack, need not be considered as stochastic variables in the prediction of risk of rail break where the pre-existing rail head cracks are closely spaced as is typical for a curve with head checks. This simplification is applied in the simulations in Section 6.

However, in the event of sparsely distributed rail head cracks in a section of track with low support stiffness (such as in a section with a few adjacent voided sleepers), the impact position (occurring once per wheel revolution) relative to the position of the crack should be considered as a stochastic variable. This was done when evaluating the risk for an instant rail break initiated at a pre-existing rail foot crack where the bending moment is much more influenced by the impact position, see Ref. [12].

5.3. Mapping of wheel flat depth distribution

For a given wheel flat geometry, the magnitude of the generated impact load is dependent on (for example) track support stiffness, wheelset (unsprung) mass, vehicle speed and axle load. For the baseline track model (corresponding to the estimated support stiffness conditions in the WILD at *Sunderbyn*, i.e., $k_b = 60$ kN/mm and $k_p = 120$ kN/mm) and the given specification of representative traffic conditions (half unsprung mass 712.5 kg, axle load 20 tonnes and speed 100 km/h), the dashed blue line in Fig. 10(a) shows the calculated influence of wheel flat depth on the wheel–rail dynamic load. In the following, this curve will be used to map a given measured dynamic load to the corresponding depth d of a discrete wheel tread surface irregularity described by Eq. (9). Thus, irrespective of the type of discrete tread surface irregularity (material fall-out, wheel flat, etc.) that generated a given measured dynamic load, its shape will be approximated by the simplified geometry shape as defined by d and l in Eq. (9).

In this way, based on a measured *distribution* of dynamic loads (see

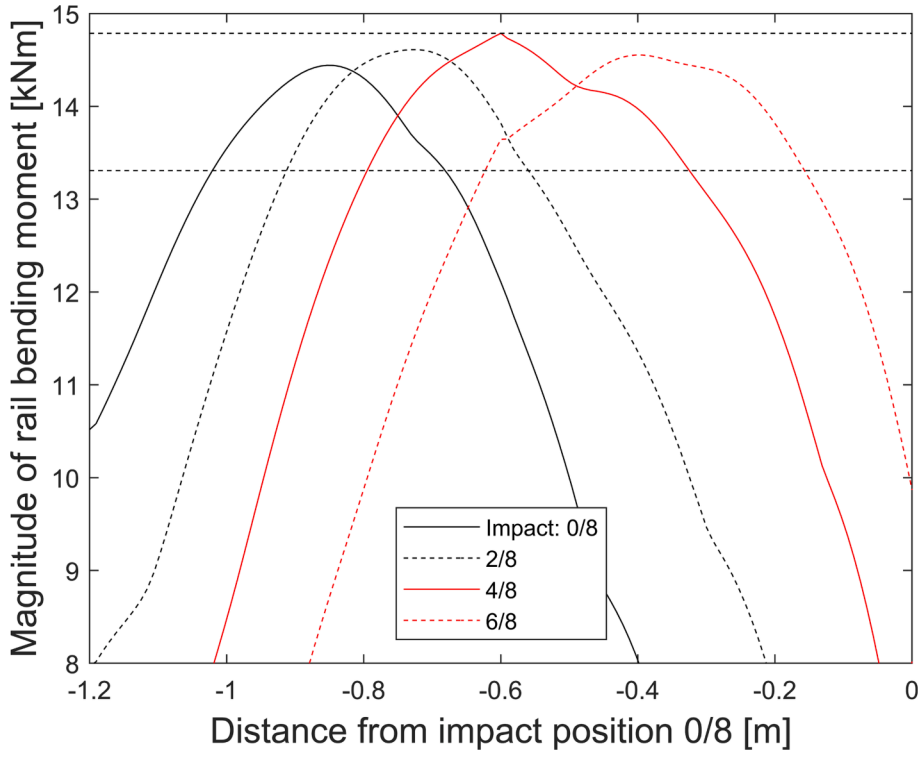

Fig. 11. Influence of distance between position of impact and position where rail bending moment was evaluated on magnitude of minimum rail bending moment. Axle load 20 tonnes, train speed 100 km/h, ballast/subgrade stiffness 60 kN/mm and wheel flat depth 1 mm.

Fig. 5), a representative *distribution* of depths of discrete wheel tread surface irregularities is generated. On a section of track with similar properties as in the *Sunderbyn* WILD and with similar vehicle properties, this distribution of irregularities should generate a similar distribution of dynamic loads as in the *Sunderbyn* WILD. However, if the same representative distribution of discrete wheel surface irregularities is applied on another track section with, e.g., a different ballast/subgrade stiffness, or if the axle load or train speed is different, a different distribution of dynamic loads would be generated. For the given distribution of wheel tread surface irregularities, this approach allows for studies of the relative influence of, *e.g.*, increasing the axle load or train speed.

It could (rightly) be argued that the same wheel tread irregularity passing through the same WILD on repeated occasions at similar speed and axle load would result in different measured dynamic loads depending on the lateral contact position on the wheel and the impact position within the WILD. However, a similar scatter in lateral wheel–rail contact positions is expected to occur also on the rest of the line, which makes the approach viable.

5.4. Meta-model of rail bending moment

Based on the mapping function for $k_b = 60$ kN/mm (axle load 20 tonnes and speed 100 km/h), see Fig. 10(a), the model described in Section 5.1 has been applied to calculate the influences of ballast/subgrade stiffness and dynamic wheel load on minimum rail bending moment. According to the procedure described in Section 5.3, this mapping function has been applied to mimic the distribution of depths of discrete wheel irregularities evaluated from the *Sunderbyn* measurements. However, in each simulation of minimum rail bending moment carried out for different combinations of irregularity depth and ballast/subgrade stiffness, the axle load was increased to 25 tonnes (the influence of axle load will be considered in Section 6).

Bending moments were calculated for a uniform grid where ballast/subgrade stiffness was varied from 10 to 100 kN/mm (sampling interval 10 kN/mm) and dynamic wheel load from 0 to 450 kN (sampling interval 25 kN). For each grid point combination, the (longitudinal) centre of the tread irregularity was aligned with a sleeper position, while the rail bending moment was sampled at intervals of $L/64$. The grid points and calculated minimum rail bending moments are indicated by the asterisks in Fig. 12. As expected, the magnitude of the minimum rail bending moment increases with increasing dynamic load (corresponding to an increased irregularity depth). The influence of ballast stiffness is moderate although there is a trend towards increasing bending moments with decreasing ballast stiffness in particular for higher dynamic loads.

For a fast numerical assessment of the bending moment for other combinations of ballast stiffness and dynamic load than those specified by the grid points, a *meta*-model of the surface in Fig. 12 has been developed based on radial basis functions using third-order poly-harmonic splines [31,32]. To reduce computational cost, this *meta*-model is applied when evaluating the performance function in Section 5.5.

5.5. Meta-model of performance function

The probability of the rare event of an instant rail break corresponds to the probability of a wheel impact load inducing a stress intensity at the pre-existing rail head crack that exceeds the fracture toughness. Based on Eq. (7), the performance function g is defined as

$$g(\theta_1, \theta_2, \cdots, \theta_M) = K_{\mathrm{Ic}} - K_{\mathrm{IT}} - \max_t\{K_{\mathrm{IB}}\} \tag{11}$$

where θ_i, $i = 1, 2, \ldots M$, are stochastic variables with prescribed cumulative distribution functions $\Phi(\theta_i)$. If $g < 0$ the rail is considered as being failed (instant rail break). Considering the distributions of variables θ_i, the probability of failure P_f is determined as the probability of $g < 0$. The hyper-surface defined by $g = 0$ is the limit state.

The computational cost for carrying out the probability analysis is reduced significantly by using a *meta*-model $\widehat{g} = f(\theta_1, \theta_2, \cdots, \theta_M)$ of the performance function g. In this way, g need not be explicitly evaluated

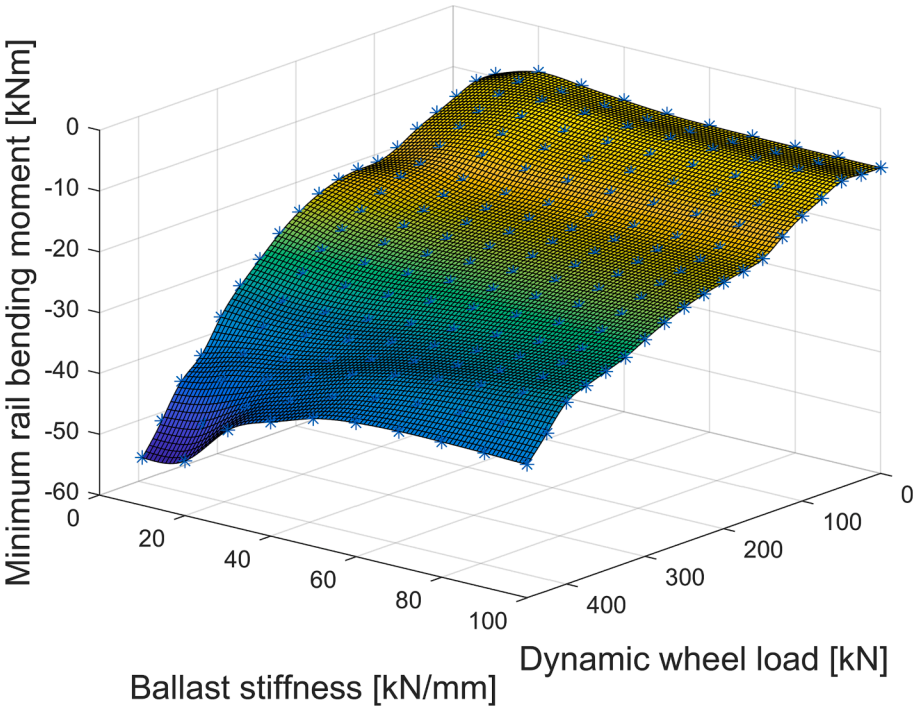

Fig. 12. Meta-model of the influence of ballast/subgrade stiffness and dynamic wheel load on minimum rail bending moment. Based on wheel flat geometry mapping function in Fig. 10(a) (k_b = 60 kN/mm). Axle load 25 tonnes.

for every new setting of the stochastic variables. Based on the cumulative distributions $\Phi(\theta_i)$, $i = 1, 2, \ldots, M$, the *meta*-model is based on a grid sampling approach. As in Section 5.4, radial basis functions using third-order poly-harmonic splines [31] are employed. An iterative process is applied, where the added samples in the next iteration step are concentrated around the limit state and fail region (i.e. where $g \leq 0$) to reduce the error in the domain that is significant for evaluating the probability of failure [12]. Before the iterative process is started, an initial screening of the performance function over the stochastic space is performed using a 11 × 11 grid of equidistant samples between 0 and 1 for each pair of variables. In each iteration, the minimum and maximum sample values of each variable $\Phi(\theta_i)$ leading to $g < 0$ are determined. In the subsequent iteration, the boundaries of the new grid are based on these sample values but extended by one grid point in each direction to include the limit state. On the reduced stochastic space, the distance between evaluated samples of $\Phi(\theta_i)$ is halved compared to the previous grid. In this way, the domain where $g < 0$ is evaluated in increasing detail. In this paper, four iterations have been used leading to that g is sampled on each cumulative distribution [0,1] down to an interval of 1/80 in the domain where $g < 0$.

5.6. Probability of failure

In this study, the subset simulation (SS) algorithm [33] has been used to calculate the probability of a rail break. It employs a multi-level Markov chain Monte Carlo (MCMC) sampling technique to adaptively generate samples from the (rare event) fail region(s) in the stochastic parameter space. The SS algorithm breaks down the rare event problem into a sequence of more frequent-nested events. The failure probability is then determined as a product of conditional probabilities, each being estimated by a MCMC simulation. As an alternative, a standard Monte Carlo simulation approach could be applied, but generally at a higher computational cost.

6. Demonstration of the simulation procedure

To demonstrate the procedure presented in this paper, the probability of a rail break is first estimated for a scenario involving the freight traffic load spectrum in Fig. 4(b). To limit the study, $M = 3$ stochastic variables are considered:

- θ_1 – dynamic load following a three-parameter Burr empirical distribution according to Fig. 5
- θ_2 – crack depth following the empirical cumulative distribution in Fig. 7
- θ_3 – fracture toughness following a normal (Gaussian) distribution, see Section 4

Other parameters, such as axle load, train speed and track stiffness, which are known to be stochastic, were considered of less influence and specified as deterministic with axle load 25 tonnes and train speed 100 km/h.

The Burr type XII distribution that was fitted to the March 2018 WILD measurements of dynamic wheel loads for freight traffic ('right wheel', see Fig. 5), and assuming that $\Phi(\theta_1 = 350\text{kN}) = 1.0$, has been applied. Then, based on the mapping function between dynamic load and wheel flat depth calculated for the baseline track model with k_b = 60 kN/mm, see Fig. 10(a), a corresponding distribution of wheel flat depths was determined. Further, the cumulative distributions for crack depths (including the rare event of an extreme crack depth up to 15.0 mm) and the fracture toughness distribution described in Section 4 were considered.

The risk of a rail break is evaluated for four different rail temperature differences ΔT = 35, 40, 45 and 50 °C and for 10 different ballast/subgrade stiffnesses k_b (per half sleeper) in the interval 10 – 100 kN/mm. For each combination of ΔT and k_b, the performance functions corresponding to 10 samples of crack depth distributions are evaluated. Based on each generated performance function, the probability of a rail break is evaluated using 10 runs with the subset simulation algorithm.

One example of the generated *meta*-model $\hat{g}$ of the performance

function is presented as three views in Fig. 13. It is observed that $\widehat{g} < 0$ only in a very small subset of the stochastic space. This is where the dynamic load and crack depth are near their maxima and the fracture toughness is near its minimum.

The evaluated influence of ΔT and k_b on the risk of a rail break (probability of failure, P_f) is summarized in Fig. 14. As expected, it is observed that the risk of a rail break increases with decreasing rail temperature (increasing ΔT) and decreasing ballast/subgrade stiffness, cf. Fig. 12. For $\Delta T \leq 35$ °C and k_b greater than 40 kN/mm, the simulated probability of failure was zero, implying that no immediate fracture would occur for cracks with depths up to 15 mm. Note that this does not imply that existing cracks will not grow under this load. Note also that the label on the vertical axis in Fig. 14 should be interpreted as the predicted probability of an event leading to an instant rail break. For example, if it is assumed that each wheel generates one severe impact load per revolution, then the probability $P_f = 1{\cdot}10^{-7}$ would correspond to one rail break in $D_w = 2\pi R_w/P_f \approx 28\,000$ km ($R_w = 0.45$ m) rolling distance. Consequently, for one freight train with N_w wheelsets, this would resemble a travelled distance of D_w/N_w. If further stochastic variables would have been added in this simulation, such as impact position relative to the position of an extreme rail head crack, the evaluated risk would be lower.

In a second demonstration example, the influence of traffic type on the risk of a rail break at rail temperature difference $\Delta T = 50$ °C is studied, see Fig. 15. The input data for the iron ore vehicle model are the same as for the freight vehicle with the following three exceptions: half unsprung wheelset mass $M_w = 670$ kg, wheelbase 1.78 m and vehicle speed 60 km/h. For the freight vehicle model, three axle loads are considered, 20, 22.5 and 25 tonnes, while two axle loads are studied for the iron ore vehicle model, 30 and 32.5 tonnes. For the iron ore vehicle, the dynamic load distribution from Fig. 5 ('right wheel') is applied with $\Phi(\theta_1 = 200\text{kN}) = 1.0$. The same 10 samples of crack depth distributions are applied for all analyses. For each ballast/subgrade stiffness k_b, presented risk values in Fig. 15 are the average taken from 100 simulations (10 crack depth distributions and 10 runs on each corresponding performance function).

For a given traffic type, it is seen that the risk of a rail break increases with increasing axle load as expected. However, it is also observed that the risk of an immediate rail break is significantly lower for the iron ore traffic despite the higher axle loads. This is because the wheels in the iron ore fleet are in better condition compared to the wheels in the freight fleet, cf. the WILD measurements reported in Figs. 3 and 4. Further, the vehicle speed is lower.

7. Conclusions

A procedure to simulate the probability of an instant rail break initiated from a pre-existing rail head crack in a continuously welded rail subjected to combined bending and temperature loading, while considering a scenario of freight traffic with a representative proportion of out-of-round wheels, has been presented. To reduce the computational costs for predicting the probability of such a rare event, *meta*-models based on poly-harmonic splines and a subset simulation algorithm considering a multi-dimensional stochastic parameter space have been applied. These *meta*-models have been used to evaluate (1) the rail bending moment generated by a given dynamic load, and (2) the performance function determining whether for a given setting of the stochastic variables the rail will fail. Supported by extensive field test data, the procedure has been demonstrated by simulating the influences of rail temperature difference ΔT, ballast/subgrade stiffness k_b, train speed and axle load.

It is argued that the presented simulation procedure can provide a scientific foundation for improved regulations for, and management of wheel tread surface irregularities. For a given traffic scenario, and with measured distributions of dynamic loads and rail head crack depths, the approach could be applied to specify alarm limits in terms of maximum

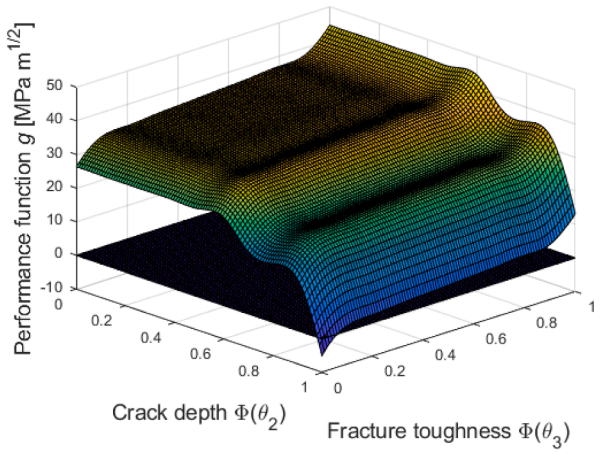

(a)

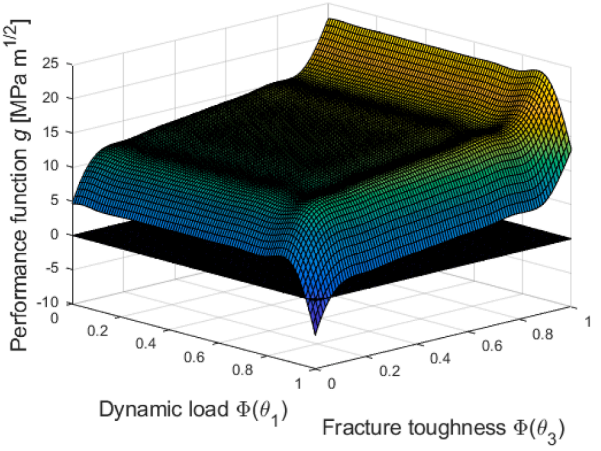

(b)

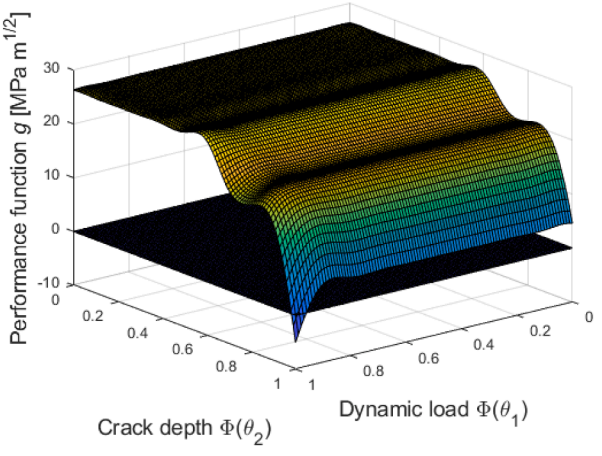

(c)

Fig. 13. *Example of meta-model of performance function $\widehat{g}$ evaluated for cumulative distributions of dynamic load (according to Fig. 5 but with maximum load 350 kN), crack depth and fracture toughness. $\Delta T = 50$ °C, $k_b = 30$ kN/mm, and crack depth distribution sample 8 with maximum crack depth 13.8 mm. Freight traffic model with axle load 25 tonnes and train speed 100 km/h. Three views: (a) $\Phi(\theta_1) = 1.0$, (b) $\Phi(\theta_2) = 1.0$, and (c) $\Phi(\theta_3) = 0.0$.*

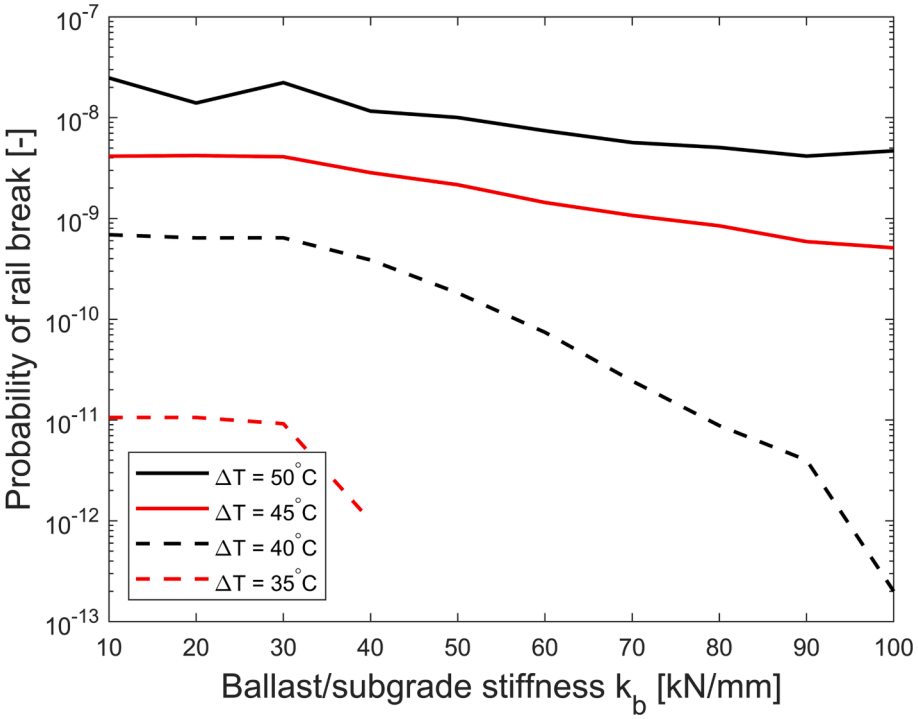

Fig. 14. *Example of evaluated influences of ΔT and k_b on probability of rail break. Freight traffic model with axle load 25 tonnes and train speed 100 km/h. Dynamic load distribution according to Fig. 5 (freight traffic, 'right' wheel) with maximum load 350 kN,* i.e. $\Phi(\theta_1 = 350kN) = 1.0$.

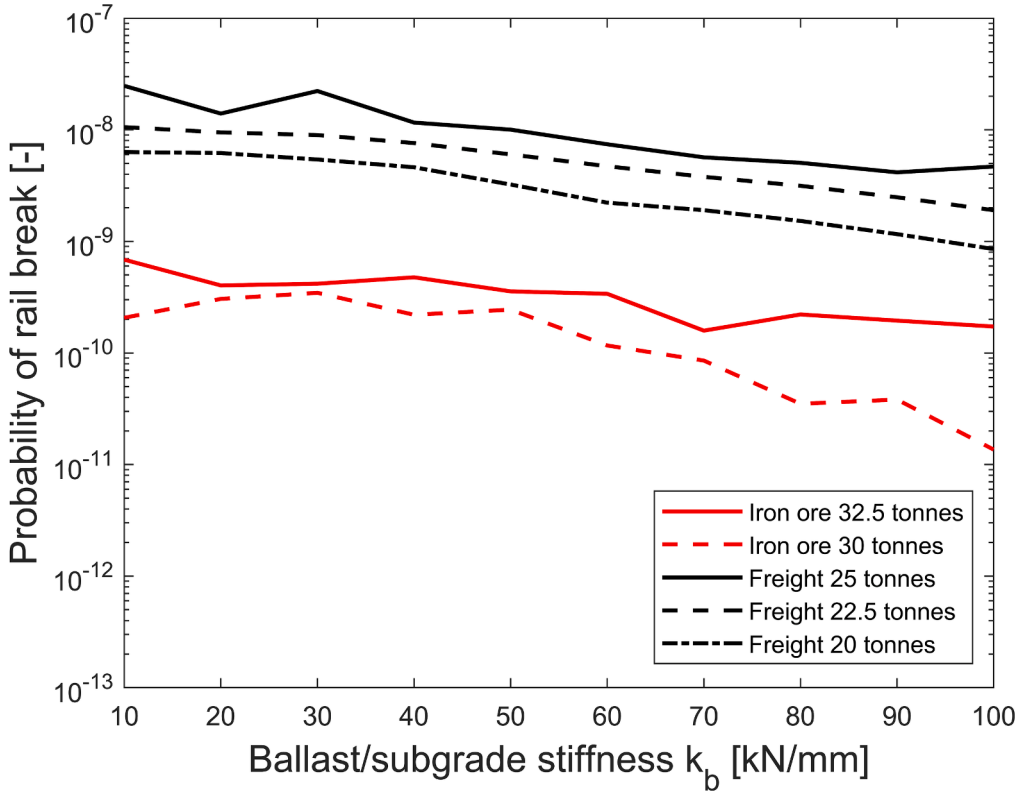

Fig. 15. *Example of evaluated influences of traffic type and k_b on probability of rail break. Freight traffic model with axle load 20, 22.5 or 25 tonnes and train speed 100 km/h. Iron ore traffic model with axle load 30 or 32.5 tonnes and train speed 60 km/h. Freight traffic: $\Phi(\theta_1 = 350kN) = 1.0$, iron ore traffic $\Phi(\theta_1 = 200kN) = 1.0$. $\Delta T = 50\,^{\circ}C$.*

allowed impact load as well as rail monitoring and maintenance strategies towards cost-efficient, safe, and reliable railway operations with a minimum of traffic disruptions.

CRediT authorship contribution statement

Jens C.O. Nielsen: Conceptualization, Methodology, Software,

Validation, Formal analysis, Writing – original draft, Project administration. **Anders Ekberg:** Conceptualization, Writing – original draft, Funding acquisition.

Declaration of Competing Interest

The authors declare the following financial interests/personal relationships which may be considered as potential competing interests: JENS NIELSEN reports financial support was provided by Horizon 2020 European Innovation Council Fast Track to Innovation. ANDERS EKBERG reports financial support was provided by Horizon 2020 European Innovation Council Fast Track to Innovation.

Data availability

Data will be made available on request.

Acknowledgments

The current work is part of the activities within the Centre of Excellence CHARMEC (CHAlmers Railway MEChanics, www.chalmers.se/charmec). Parts of the study have been funded within the European Union's Horizon 2020 research and innovation programme in the Shift2Rail projects In2Track2 and In2Track3 under grant agreement nos. 826255 and 101012456. The authors are grateful to Matthias Asplund, Simon Barthelemy, Stefan Kallander, Magnus Svensson and Malin Syk, Trafikverket (the Swedish Transport Administration), for providing input data.

References

[1] Cannon DF, Edel K-O, Grassie SL, Sawley K. Rail defects: An overview. Fatigue Fract Eng Mater Struct 2003;26(10):865–86.
[2] Ekberg A, Kabo E (Eds). Surface fatigue initiated transverse defects and broken rails – An international review. *Research report 2014:05*. Department of Applied Mechanics, Chalmers University of Technology, Gothenburg, Sweden, 2014, 22 pp.
[3] Marais JJ, Mistry KC. Rail integrity management by means of ultrasonic testing. Fatigue Fract Eng Mater Struct 2003;26(10):931–8.
[4] Ekberg A, Kabo E. Lundén R Rail and wheel health management. Wear 2023: 204891. https://doi.org/10.1016/j.wear.2023.204891.
[5] Magel E, Mutton P, Ekberg A, Kapoor A. Rolling contact fatigue, wear and broken rail derailments. Wear 2016;366:249–57.
[6] Kaewunruen S, Remennikov AM. Progressive failure of prestressed concrete sleepers under multiple high-intensity impact loads. Eng Struct 2009;31(10): 2460–73.
[7] Ferreño D, Casado JA, Carrascal IA, Diego S, Ruiz E, Saiz M, et al. Experimental and finite element fatigue assessment of the spring clip of the SKL-1 railway fastening system. Eng Struct 2019;188:553–63.
[8] Yan R-G, Wang W-J, Guo Y-T, Liu X-L, Wu S-C, Zhang Z-X. Influence of wheel out-of-roundness on the remaining life of railway wheels under mixed-mode fatigue loading. Fatigue Fract Eng Mater Struct 2022;45(7):2072–85.
[9] Maglio M, Vernersson T, Nielsen JCO, Ekberg A, Kabo E. Influence of railway wheel tread damage on wheel–rail impact loads and the durability of wheelsets. Railway Engineering Science 2023. https://doi.org/10.1007/s40534-023-00316-2.
[10] Yang Y, Ling L, Wang C, Liu Z, Wang K, Zhai W. Wheel/rail dynamic interaction induced by polygonal wear of locomotive wheels. Veh Syst Dyn 2022;60(1): 211–35.
[11] UIC: Prevention and mitigation of derailment (PMD), IRS 70729, 2019.
[12] Nielsen JCO, Abrahamsson TJS, Ekberg A. Probability of instant rail break induced by wheel-rail impact loading using field test data. International J Rail Transportation 2022;10(1):1–23.
[13] Johansson A, Nielsen JCO. Out-of-round railway wheels - Wheel–rail contact forces and track response derived from field tests and numerical simulations. Proc Instn Mech Engrs Part F: J Rail Rapid Transit 2003;217:135–46.
[14] Nielsen JCO, Kabo E, Ekberg A. Larmgräns för hjulskadedetektorer – En utredning av risk för rälbrott på Malmbanan (Alarm limit for wheel impact load detectors – An investigation of risk for rail break on Malmbanan. In: Swedish) *Research report 2007:05* Department of Applied Mechanics, 40. Gothenburg, Sweden: Chalmers University of Technology; 2007. pp..
[15] Schenck Process. MULTIRAIL WheelScan. [cited 2023 June 20]. Available from: https://www.schenckprocess.com/products/wheel-diagnosis-wheelscan.
[16] Burr IW. Cumulative frequency functions. Ann Math Stat 1942;13(2):215–32.
[17] Sandström J, Ekberg A. Predicting crack growth and risks of rail breaks due to wheel flat impacts in heavy haul operations. Proc Instn Mech Engrs Part F: J Rail Rapid Transit 2009;223:153–61.
[18] Ekberg A, Kabo E, Nielsen JCO. Allowable wheel loads, crack sizes and inspection intervals to prevent rail breaks. In: *Proceedings. 11th International Heavy Haul Conference*, Perth, Australia, 2015, 9 pp.
[19] Ekberg A, Kabo E. Fatigue of railway wheels and rails under rolling contact and thermal loading – An overview. Wear 2005;258(7-8):1288–300.
[20] voestalpine Railway Systems, voestalpine AG, Austria, Rainer Hochfellner, April 2021, (private communication).
[21] Liu Y, Tsang KS, Hoh HJ, Shi X, Pang JHL. Structural fatigue investigation of transverse surface crack growth in rail steels and thermite welds subjected to in-plane and out-of-plane loading. Eng Struct 2020;204:110076.
[22] Nielsen JCO, Berggren E, Hammar A, Jansson F, Bolmsvik R. Degradation of railway track geometry – Correlation between track stiffness gradient and differential settlement. Proc Instn Mech Engrs Part F: J Rail Rapid Transit 2020;234 (1):108–19.
[23] Nielsen JCO, Pieringer A, Thompson DJ, Torstensson PT. Wheel–rail impact loads, noise and vibration: A review of excitation mechanisms, prediction methods and mitigation measures. Notes on Numerical Fluid Mechanics and Multidisciplinary Design 2021;150:3–40.
[24] Nielsen JCO, Igeland A. Vertical dynamic interaction between train and track – Influence of wheel and track imperfections. J Sound and Vibration 1995;187(5): 825–39.
[25] Nielsen JCO. High-frequency wheel–rail contact forces – Validation of a prediction model by field testing. Wear 2008;265:1465–71.
[26] Wu TX, Thompson DJ. A hybrid model for the noise generation due to railway wheel flats. J Sound and Vibration 2002;251(1):115–39.
[27] Nielsen JCO, Lombaert G, François S. A hybrid model for prediction of ground-borne vibration due to discrete wheel/rail irregularities. J Sound and Vibration 2015;345:103–20.
[28] Newton SG, Clark RA. An investigation of the dynamic effects on track of wheelflats on railway vehicles. J Mech Eng Sci 1979;21(4):287–97.
[29] Pieringer A, Kropp W, Nielsen JCO. The influence of contact modelling on simulated wheel/rail interaction due to wheel flats. Wear 2014;314(1-2):273–81.
[30] Nielsen JCO, Oscarsson J. Simulation of dynamic train–track interaction with state-dependent track properties. J Sound and Vibration 2004;275(3-5):515–32.
[31] Fasshauer GE. Meshfree approximation methods within Matlab. In: *Interdisciplinary Mathematical Sciences*. – 2007;6. New Jersey: World Scientific Publishing.
[32] Wiens T. Radial basis function network (https://www.mathworks.com/matlabcentral/fileexchange/22173-radial-basis-function-network), MATLAB Central File Exchange. Retrieved June 3, 2022.
[33] Au S-K, Beck JL. Estimation of small failure probabilities in high dimensions by subset simulation. Prob Eng Mech 2001;16(4):263–77.